IL NUOVO CIMENTO Online First
DOI 10.1393/ncb/i2010-10909-0

Basic topics: Experimental Techniques and Instruments

# Measurements of photon dectection efficiency of Geiger-mode avalanche photodiodes (G-APD)

S. Gentile([1]), E. Kuznetsova([2]) and F. Meddi([1])

([1]) *Università di Roma "La Sapienza" - Piazzale Aldo Moro 5, 00185 Rome, Italy*
([2]) *DESY - Notkestraße 85, 22607, Hamburg, Germany*

(ricevuto il 10 Maggio 2010; revisionato il 5 Luglio 2010; approvato il 17 Luglio 2010; pubblicato online il 21 Settembre 2010)

**Summary.** — An estimation of the photon detection efficiency of multi-pixel Geiger-mode avalanche photodiodes based on measurements of their response to low-intensity light is presented. Properties of detectors manufactured by different producers are compared. A new fit method of the response spectra to light, taking into account after-pulse and cross-talk effects is proposed to yield the initial number of photons. The value of photon detection efficiency is calculated using a calibrated photodetector as a reference. The sources of systematic error are discussed.

PACS 29.40.Wk – Solid-state detectors.
PACS 07.85.Fv – X- and $\gamma$-ray sources, mirrors, gratings, and detectors.
PACS 85.60.Gz – Photodetectors (including infrared and CCD detectors).

## 1. – Introduction

Multi-pixel Geiger-mode avalanche photodiodes (G-APDs) are solid-state photodetectors based on a technology developed since early 1990's [1-7]. Their gain is typically $10^6$ per photoelectron. Their main features are: the small size, the efficiency comparable to the one of vacuum photomultipliers, the insensitivity to magnetic field, a low bias voltage and a reasonable price. These advantages led in the last decade to an intense development by different institutions and manufacturers which resulted in a great improvement of the technology. As a result, a number of different types of G-APD are currently available on the market, also under the name of Silicon Photo-Multiplier (SIPM) or Multi-Pixel Photon Counter (MPPC). We will use the generic name G-APD for any of them.

Currently, the G-APDs find an application in many fields of physics, High-Energy [8-10], Neutrino [11] and Astroparticle [12-14], and in Medicine [15].

This work describes a comparative study performed in the same experimental conditions, on different G-APDs, to allow an optimal choice with a view to a given application. Measurements of a G-APD response to low-intensity light have been carried on to determine the main characteristics, particularly the Photon Detection Efficiency (PDE). To this purpose we performed an accurate fit of the G-APD response spectra also yielding

 

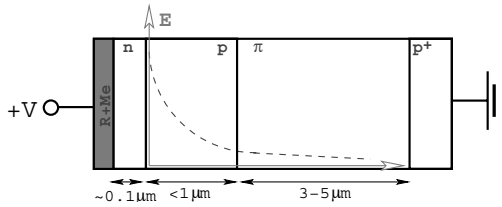


Fig. 1. – Schematic view of a G-APD microcell. From left, are shown: the resistive layer, the $n$ layer, the three $p$ layers with different doping ($p$, $\pi$, $p^+$). The absorption of photons (and then the photogeneration) takes place mainly in the layer $\pi$. $E$ indicates the electric field and $V = V_{\rm bias}$ is the reverse bias [3].

the after-pulse and cross-talk contributions, and we compared it with the one from a calibrated reference photodetector.

This paper is organized as follows. First, the G-APD main characteristics are reviewed (sect. **2**), then the experimental setup (sect. **3**), the samples (sect. **4**) and the fitting method (sect. **5**) are described. The measurements of the G-APD samples are discussed (sects. **6** to **7**) and the conclusions are drawn (sect. **9**).

## 2. – General principle of the G-APD operation and its characteristics

We would like to summarize the general principle of G-APD operation and the main characteristics, without claiming to be exhaustive, but referring to elsewhere for a review [8].

A G-APD consists of a large number of identical microcells (silicon diodes, pixels) with a common anode, like the one sketched in fig. 1. The microcells are located on a common substrate with a typical size of $\sim 1 \times 1\,\mathrm{mm}^2$. Under a reverse bias, $V_{\rm bias}$, above the breakdown voltage, $V_{\rm brd}$, the multilayer structure with different doping concentrations provides a high gradient of electric field in the vicinity of the $n$-$p$ junction region. The electrons (photoelectrons) created via photoabsorption in the $\pi$-region drift toward the $p$-layer where the avalanche multiplication occurs. The resistive layer on the top of the $n$-side provides a voltage drop during the avalanche development due to the growing current. This causes a redistribution of the potentials bringing the G-APD voltage down to the breakdown value, $V_{\rm brd}$, when the avalanche is quenched. Thus the charge induced during the avalanche discharge is proportional to the overvoltage ($V_{\rm over} = V_{\rm bias} - V_{\rm brd}$), $Q = V_{\rm over} \times C$, where $C$ is the junction capacitance [3, 16].

At a high voltage, in a generic photodiode, the avalanche is turned into Geiger mode discharge. In this mode, the device response does not depend on the initial number of photoelectrons. In G-APD the proportionality has been restored with the splitting of the device into a large number of independent pixels connected to the same output. Then, it is impossible to identify inside the G-APD the diode producing the signal, since all diodes are connected to the same output. The number of fired pixels is proportional to the initial number of photoelectrons, as long as it is small in comparison with the total number of pixels in the G-APD. This implies a low-intensity light source in the measurement setup.

The gain ($g$) is determined by the charge released in one pixel, which is proportional to the pixel capacitance, as we have mentioned before. With standard parameters, one photoelectron produces $\sim 10^6$ electrons. Then, the relative gain variation ($\Delta g/g$) is

proportional to the relative variation of the bias voltage ($\Delta V_{\rm bias}/V_{\rm bias}$). Therefore, a G-APD operating at low voltage has a larger gain sensitivity to the voltage variation and requires a better voltage stabilization. These characteristics demand a high-voltage stabilization in the setup design.

As in all solid-state electronic devices, the G-APD performances are depending on temperature. The most notable temperature dependence is observed in gain and in noise rate. The dependence of noise rate on temperature can be easily understood in terms of electron-hole pairs randomly created through thermal generation (dark rate). These thermal charges can fire the cells and create signals independently of the presence of incident photons. This has been taken into account in the setup design.

Other characteristics of the G-APD response to light deserve a few words.

After-Pulses (AP) appear when the quenching (mechanism to stop the avalanche process by temporally reducing the cell voltage) does not drain all the charge in the sensitive area, and the cell fires again shortly after the original pulse. After-pulses originate from a fraction of carriers generated in an avalanche and subsequently trapped in lattice defects, to be released later with the characteristic time constant, when the discharge is already quenched. These re-emitted carriers might trigger another sequence of Geiger discharges. The after-pulses coming soon, after the initial signal, have a smaller amplitude, since the pixel had no sufficient time to completely recharge. Obviously, this effect is proportional to the number of electrons in the discharge (*i.e.* gain) and to the probability of triggering the Geiger discharge. Therefore, it is depending on $V_{\rm bias}$.

Cross-talk takes place when in a Geiger discharge, some of the electrons generated in the avalanche process reach the adjacent pixel, where another Geiger discharge might be triggered. This results in a pulse with a larger amplitude (nearly a factor two) and in a distortion of the linear response of the device. Thus, the cross-talk is one of the critical issues to be minimised in G-APD. This effect has two components corresponding to electrons produced in the pixel active region (prompt) and in the bulk (delayed). The first one can be suppressed by trenches between pixels, the second one by additional $p$-$n$ junctions.

Photon detection efficiency, PDE, is one of the most important parameters of a photon detector. Every detector can only convert a certain percentage of incident photons in signals. This G-APD efficiency is given as a product of three factors:

$$\mathrm{PDE} = QE \times \epsilon_{\rm geom} \times \epsilon_{\rm Geiger}, \tag{1}$$

where $QE$ is the G-APD quantum efficiency, and depends on the incident photon wavelength, $\lambda_w$; $\epsilon_{\rm geom}$ is a geometrical factor (fill factor) indicating which fraction of the device is sensitive to photons; $\epsilon_{\rm Geiger}$ is the probability to trigger a Geiger discharge and is a function of $V_{\rm bias}$. PDE decreases with the pixel size.

The G-APD response can be written as a product of few factors:

$$A = N_\gamma^{\rm in} \times \mathrm{PDE} \times g \times (1+\varepsilon) \times (1+P_{\rm AP}), \tag{2}$$

where $N_\gamma^{\rm in}$ is the number of incident photons; $g$, the gain; $\varepsilon$, the cross-talk probability and $P_{\rm AP}$, the after-pulse probability. It should be noticed that in the above equation, $g$, PDE, $\varepsilon$ and $P_{\rm AP}$ are all increasing with $V_{\rm bias}$, implying a complex dependence of the G-APD response on the bias voltage.

The previous considerations have driven the experimental setup design and the measurement strategy.

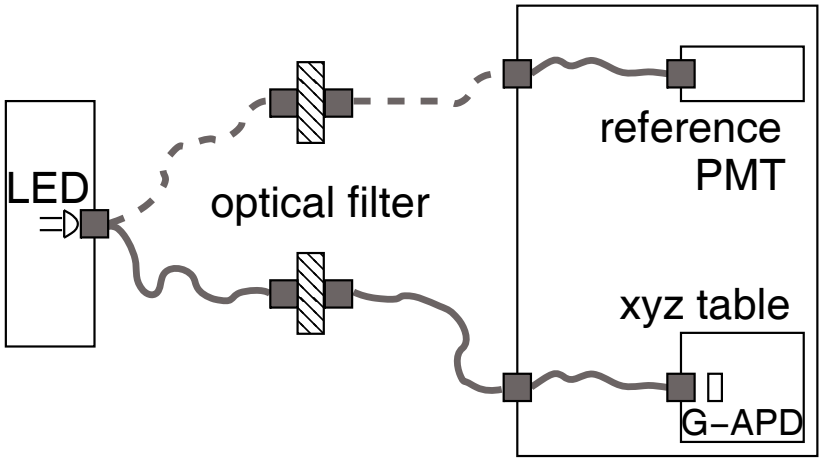


Fig. 2. – General scheme of the PDE measurements.

## 3. – Measurement setup

Figure 2 shows the scheme of the PDE measurements. The light from a Light-Emitting Diode (LED) operating in a pulse-mode with a Waveform Generator (AGILENT 33220A) was delivered to an optical filter. The latter corresponded to the peak wavelength of the LED and had a bandwidth of ±3 nm. By changing the LED, a few wavelengths in the 380–650 nm range were investigated. For low intensity sources (380 nm, 400 nm, 565 nm) the LED light was not filtered.

The filtered light was routed to a light-tight thermostabilized box with two photodetectors: the G-APD and the reference photodetector. The box temperature was controlled at ±0.1 °C during the data taking. As a reference photodetector a PhotoMultiplier Tube (PMT) H5783P produced and calibrated (for this reference) by HAMAMATSU was used. Table I shows for each wavelength $\lambda_w$: the efficiency of the reference photodetector for the peak wavelength, $\epsilon^{\mathrm{ref}}_{\mathrm{peak}}$, as provided by the manufacturer; the filter bandwidth, BW; the LED full width half maximum, FWHM; the efficiency of the reference device, $\epsilon^{\mathrm{ref}}_{\mathrm{eval}}$, as evaluated for our light source.

Both PMT and G-APDs have effective areas (Ø 8 mm and $1 \times 1\,\mathrm{mm}^2$, respectively) much larger than the fiber core (diameter = 50 $\mu$m). The reference PMT has an FC type fiber adapter providing a reliable optical coupling between the fiber and PMT window at a distance of less than 5 mm. A G-APD was fixed on a movable $xyz$-stage. The distance between the fiber edge and the effective area was set to 5 mm, with a precision of ±0.1 mm.

Figure 3 shows the read-out scheme of the G-APD. The signal from G-APD is read out with a charge-sensitive preamplifier and digitized with an integrating ADC (CAEN QADC V792N). The LED pulse of about 6 ns duration and the ADC gate of about 65 ns width were synchronized by means of a common trigger. The integration time was long enough to contain most of G-APD signal. In case of the reference photodetector the direct signal from PMT was amplified with an external amplifier (NIM ORTEC 450) and digitized with the same ADC. Due to a high sensitivity to voltage variations, the G-APD bias voltage was provided by a high precise and stable in time voltage source (Keithley 6487/E).

TABLE I. – *Efficiencies of the reference photodetector, the PMT H5783P. From left: wavelength, $\lambda_w$; efficiency provided by the manufacturer Hamamatsu, $\epsilon^{\rm ref}_{\rm peak}$; filter bandwith,* BW*; source* FWHM*; efficiency as evaluated for our source, $\epsilon^{\rm ref}_{\rm eval}$.*

| $\lambda_w$ (nm) | $\epsilon^{\rm ref}_{\rm peak}$[1] (%) | BW (nm) | FWHM (source) (nm) | $\epsilon^{\rm ref}_{\rm eval}$ (%) |
|---|---|---|---|---|
| 380 | 23.46 | | ±8 | $22.98^{-0.21}_{-0.05}$ |
| 400 | 22.69 | | ±13 | $22.75^{+0.46}_{-0.10}$ |
| 450 | 20.33 | ±3 | | $20.33^{+0.27}_{-0.28}$ |
| 500 | 15.45 | ±3 | | $15.45^{+0.32}_{-0.68}$ |
| 565 | | | ±30 | $5.30^{+2.37}_{-2.63}$ |
| 600 | 2.30 | ±3 | | $2.30^{+0.19}_{-0.19}$ |
| 650 | 0.28 | ±3 | | $0.28^{+0.05}_{-0.04}$ |

## 4. – Samples

The measurements refer to the samples listed in table II. The following operating conditions were chosen:

- HAMAMATSU produced Multi-Pixel Photon Counter S10362-11-025U [17] operated at $V_{\rm bias} = 71.3\,{\rm V}$ corresponding to $V_{\rm over} \simeq 2.3\,{\rm V}$.
- CPTA produced SiliconPhotoMultiplier operated at $V_{\rm bias} = 32.5$ and $32.7\,{\rm V}$ corresponding to $V_{\rm over} \simeq 2.3\,{\rm V}$ and $2.5\,{\rm V}$. The parameter dependence on voltage has been studied in the range between 31.5 and $33.3\,{\rm V}$.
- IRST produced SiliconPhotoMultiplier operated at $V_{\rm bias} = 32.0\,{\rm V}$ corresponding to $V_{\rm over} \simeq 1.5\,{\rm V}$.

The temperature at data taking was $T \sim 23.7\,^\circ{\rm C}$ stabilized at $\pm 0.1\,^\circ{\rm C}$ during each measurement and with a spread $\pm 0.3\,^\circ{\rm C}$ during all period of data taking.

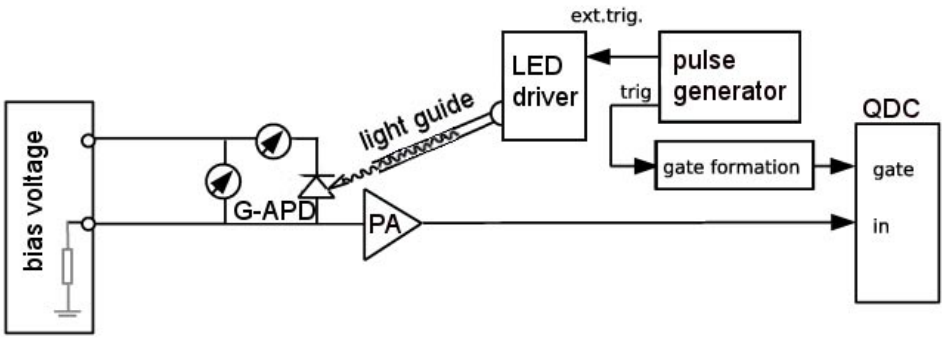


Fig. 3. – Schematic G-APD read-out.

TABLE II. – *From left: Manufacturer, type, photosensitive area, number of pixels and their pitch.*

| Sample | Type | Photosensitive area ($mm^2$) | Number of pixels | Pixel pitch ($\mu m^2$) |
|---|---|---|---|---|
| HAMAMATSU | S10362-11-025U | $1 \times 1$ | 1600 | $25 \times 25$ |
| CPTA[(1)] | 143 | 1.028[(2)] | 556 | $43 \times 43$ |
| IRST[(3)] | 2007 prod | $1 \times 1$ | 400 | $50 \times 50$ |

(1) Sample kindly provided by Prof. M. Danilov.
(2) Sensitive area has octagonal shape.
(3) Sample kindly provided by Dr. C. Piemonte (Fondazione Bruno Keller).

## 5. – Measurement strategy and fit procedure

As described in sect. **3** the PDE measurement strategy is based on the comparison of the effective number of photons detected from reference detector and G-APD.

To accomplish this task, noise and light (signal) response spectra from G-APD and PMT to a low number of photons have been measured and fitted, as described in the following.

The number of photons, $n$, detected per light pulse is expected to be Poisson distributed, with the mean value $\lambda$. This distribution has to be convoluted with a Gaussian distribution describing the experimental resolution. The charge $x$ measured by the ADC is expected to have a frequency distribution, $N(x)$:

$$N(x) = N \times (\text{Poisson}(n;\lambda) \otimes \text{Gauss}(\mu_n, \sigma_n)),$$

or, more explicitly,

$$N(x) = N \times e^{-\lambda} \sum_{n \geq 0} \left( \frac{\lambda^n}{n!} \times \frac{1}{\sigma_n} \exp\left[ \frac{-(x-\mu_n)^2}{2\sigma_n^2} \right] \right). \tag{3}$$

In the ideal case $n$ photons correspond to a charge $\mu_n = \mu_0 + n \times g$, where $\mu_0$ is the pedestal position and $g$ is the gain factor. In the presence of a finite resolution the distribution of charge follows a Gaussian distribution around each $\mu_n$ with a width $\sigma_n$, $\sigma_n^2 = \sigma_0^2 + n \times \sigma_1^2$, where $\sigma_0$ is the electronic noise (pedestal) width and $\sigma_1$ is the single-photon width. $N$ is a normalization factor.

*Reference PMT fit procedure*. In the PMT case, it should be noticed that due to additional electrical noise caused by the external amplifier, the no-light spectrum (pedestal) is described as a superposition of three Gaussian peaks, two of which are considered to be symmetric. Figure 4 (left) shows the pedestal fitted with the sum of three Gaussians. Figure 4 (right) shows the signal fitted with eq. (3) modified to include the noise shape.

Using the mean number of detected photons, $\lambda = N_\gamma^{\text{PMT}}$, as obtained from the above fit, and the PMT efficiency from table I, the mean number of photons delivered by the optical system to the photodetector surface per one LED pulse was estimated.

In the example of fig. 4, at $\lambda_w = 450\,\text{nm}$, it is $N_\gamma^{\text{PMT}} = 1.71 \pm 0.02$. Taking into account the efficiency for this $\lambda_w$, $\epsilon_{\text{eval}}^{\text{ref}} = 20.33^{+0.27}_{-0.28}\%$ (table I) the mean number of photons impacting PMT is obtained. This is the first step for the PDE calculation.

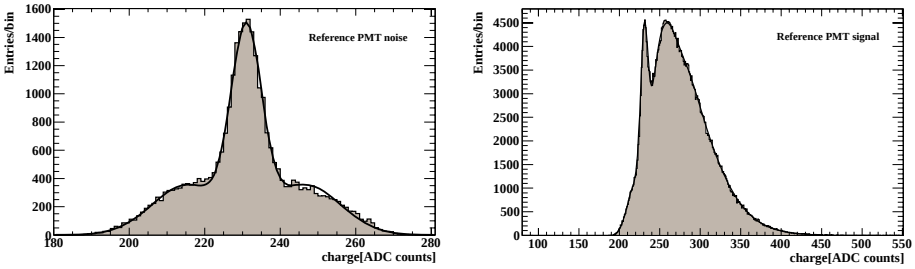


Fig. 4. – Reference PMT: noise (left) and signal (right) spectra. The signal is obtained by short, low-intensity LED flashes at $\lambda_w = 450 \pm 3\,\mathrm{nm}$. The continuous lines are the fit results (see text). From the fit the mean number of detected photons is obtained, $N_\gamma^{\mathrm{PMT}} = 1.71 \pm 0.02$ ($\epsilon_{\mathrm{eval}}^{\mathrm{ref}} = 20.33^{+0.27}_{-0.28}\%$, see text).

*G-APD fit procedure*. Figure 5 shows typical G-APD HAMAMATSU response spectra, on the left for no light (noise) and on the right for low-intensity light (signal).

The noise spectrum shows beyond the first peak (pedestal) other peaks which are due to thermogeneration. Since their contribution to the total noise is about 2% of the pedestal, the thermogeneration effect can be neglected in the signal fit. Moreover, since the probability of two or more thermogeneration counts within the gate is negligible, the cross-talk effect can be estimated from the ratio of the numbers of events in the 3rd and 2nd peak. This value ($\sim 20\%$) depends on the gate length (in our case 65 ns) and on the operation voltage, $V_{\mathrm{bias}}$ (sect. **2**).

In the signal spectrum the first peak (pedestal) corresponds to the noise, the second one is the G-APD response when exactly one photon is detected (one pixel is fired). It is impossible to identify which one of the pixels was fired, since they are all connected to the same output and they have similar responses. If $n$ pixels are fired, the sum of $n$ charges is recorded at the position of the $(n+1)$-th peak, $\mu_n = \mu_0 + n \times g$. These peaks, as shown in fig. 5 (right), are equidistant, at a distance determined by the gain factor, $g$. The enhancements which show up between the peaks, were attributed to after-pulses (AP) and were considered in the fit.

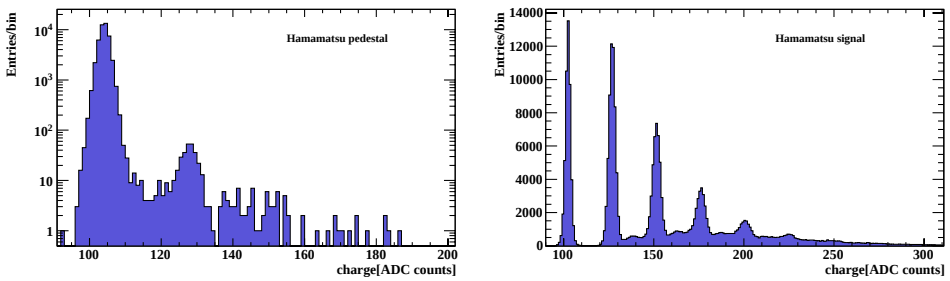


Fig. 5. – HAMAMATSU G-APD: noise (left) and signal (right) spectra. The signal is obtained by short, low-intensity LED flashes at $\lambda_w = 450 \pm 3\,\mathrm{nm}$. Each peak corresponds to a number of detected photons.

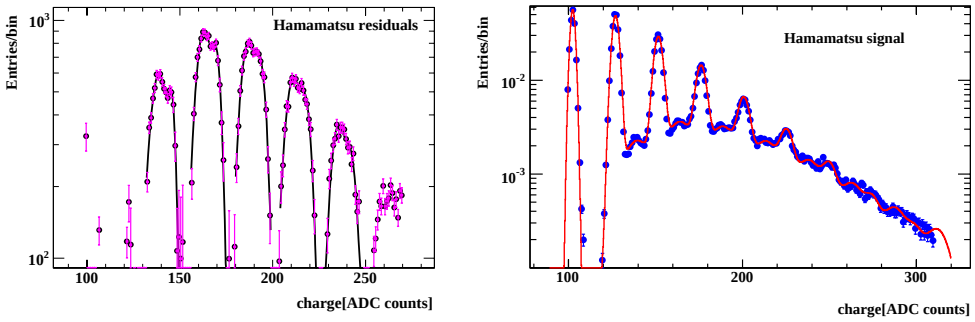


Fig. 6. – Residual distribution after subtraction of best-fitted Gaussians from the signal spectrum (left). The signal spectrum fitted with the after-pulse corrections (right). From this fit, the probability, $P_n^0$, to get $n$ cells fired and the probability, $P_{\rm AP}$, to get an after-pulse from one cell are derived (in this example $P_{\rm AP} = 0.16 \pm 0.01$).

To identify the most appropriate function describing this effect the main peaks, each fitted to a Gaussian distribution, were subtracted from the spectrum of fig. 5 (right). As a result, a sequence of peaks, fig. 6 (left), was obtained, each one well described as a sum of two Gaussians (for this G-APD and for the chosen gate length). This suggested to write a new fitting function $P(x)$ as follows.

If $P_n^0$ is the probability to get initially $n$ cells fired (the Poissonian $n$ term in eq. (3)), the probability to record an $x$ charge, $P(x) = N(x)/N$ can be written as a sum of three terms representing, respectively, the probability of an $x$ charge when $n$ cells are fired 1) without AP; 2) with a single AP from any cell; 3) with more than a single AP from any cell:

$$P(x) = \sum_n P_n^0 \Big( P_n^{\rm noAP} \times {\rm Gauss}(\mu_n, \sigma_n) + P_n^{\rm AP1} \times {\rm Gauss}(\mu_n + \delta_1, \sigma_1) + P_n^{\rm AP2} \times {\rm Gauss}(\mu_n + \delta_2, \sigma_2) \Big). \tag{4}$$

Here ${\rm Gauss}(\mu, \sigma) = \frac{1}{\sqrt{2\lambda}\sigma} \exp\left[\frac{-(x-\mu)^2}{2\sigma^2}\right]$; $\delta_{1,2}$ are the distances of the first and second after-pulse Gaussian from the nearest main peak and $\sigma_{1,2}$ the widths; the coefficients $P_n^{\rm noAP}$, $P_n^{\rm AP1}$ and $P_n^{\rm AP2}$ are all functions of a single parameter $P_{\rm AP}$, the probability to get an AP from one cell. In detail, $P_n^{\rm noAP}$ is the probability that an event with $n$ fired pixels does not contain any AP, events of this kind enter the $(n+1)$-th Gaussian peak of the G-APD spectrum, fig. 5 (right). Also the probability that an event with $n$ fired pixels containing any number of AP is $P_n^{\rm AP} = (1 - P_n^{\rm noAP}) = (1 - (1 - P_{\rm AP})^n)$; these events are responsible for the tail enhancements on the right of the Gaussian peaks (except for the pedestal peak, $n = 0$). Similarly, if $j$ is the number of fired cells with more than a single AP, one can write $P_n^{\rm AP1} = P_n^{\rm AP} \times (1 - P_{\rm AP})^j$ and $P_n^{\rm AP2} = P_n^{\rm AP} \times (1 - (1 - P_{\rm AP})^j)$. Moreover, fit studies suggest that $j \approx n$.

If the probability of after-pulses is zero, eq. (4) is equivalent to eq. (3).

Equation (4) was fitted to the spectrum of fig. 5 (right) and the fit result is shown in fig. 6 (right) as a continuous line. Among the free parameters, we obtain the $P_n^0$ values as displayed in fig. 7 (black dots) and the after-pulse probability, $P_{\rm AP} = 16\%$.

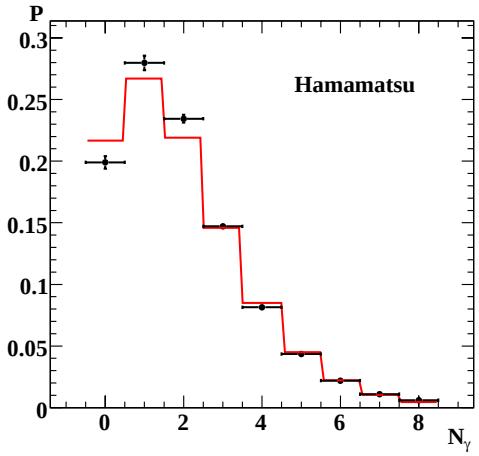


Fig. 7. – (Colour on-line) Distribution of probability, $P$, to observe $N_\gamma$ photons. The data, black dots, are the $P_n^0$ obtained by fitting the signal spectrum (fig. 6, right). The continuous (red) line represents the fit of these data with eq. (5). In this example, the fitted values are: the mean number of G-APD detected photons, $N_\gamma^{\text{G-APD}} = 1.55 \pm 0.02$, and the cross-talk probability, $\varepsilon = 0.20 \pm 0.01$. Binwidth = 1.

The $P_n^0$ values should be distributed according to the Poisson statistics with a mean number of photons detected, $N_\gamma^{\text{G-APD}}$ (corresponding to Poisson's distribution parameter $\lambda$). However this distribution is distorted by the presence of cross-talk. If the cross-talk probability is $\varepsilon \neq 0$, then the $n = 1$ bin (2nd peak in fig. 6 (right)) contains only events with one initially fired cell without any cross-talk, with a probability $P(1) = P_1^0(1-\varepsilon)$. The $n = 2$ bin (3rd peak) is filled either when two cells are initially fired without cross-talk or when one cell is fired accompanied by a second cell fired by cross-talk: $P(2) = P_2^0(1-\varepsilon)^2 + P_1^0\varepsilon(1-\varepsilon)$. Finally the probability to observe $n$ fired cells $P(n)$ can be written:

$$P(n) = \sum_{j=1}^{n} P_j^0 (1-\varepsilon)^j \varepsilon^{n-j} \binom{n-1}{j-1}. \tag{5}$$

The data in fig. 7 were fitted using eq. (5); the continuous (red) line represents the result of the fit. For these data, the value obtained for the cross-talk probability was $\varepsilon = 0.20 \pm 0.01$; the value of the mean number of detected photons is $N_\gamma^{\text{G-APD}} = 1.55 \pm 0.02$. In general, for any pair of measurements on G-APD sample, and on the reference PMT, we have

$$\text{PDE} = \frac{N_\gamma^{\text{G-APD}}}{N_\gamma^{\text{PMT}} \cdot \epsilon_{\text{eval}}^{\text{ref}}}. \tag{6}$$

With the mean number of photons detected by G-APD, $N_\gamma^{\text{G-APD}}$ and by PMT, the reference detector, $N_\gamma^{\text{PMT}}$, it is possible to evaluate the photon detection efficiency. In our example, the PDE value is $18.36 \pm 0.26\%$ (statistical error only).

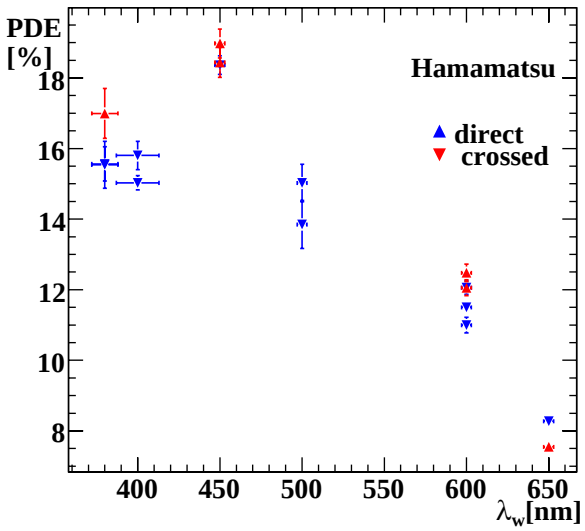


Fig. 8. – (Colour on-line) The photon detection efficiency, PDE, for HAMAMATSU G-APD as a function of the light wavelength, $\lambda_w$, for each measurement. Blue dots (▲) indicate measurements with the same fiber configuration, red dots (▼) with the swapped fiber configuration.

The final value of PDE is obtained as a mean of various measurements at different light intensities, with different fiber configurations, taking into account the FWHM of the light source and the filter bandwidth.

The procedure and results described in this section for G-APD HAMAMATSU were as well applied to the others samples, with minor modifications. In the following sections these results are discussed.

## 6. – Photon detection efficiency: Hamamatsu sample

Based on the fitting procedure of sect. **5**, it is possible to calculate for each measurement the corresponding PDE value. The measurements have been made at different light intensities and with different optical layouts to evaluate possible sources of systematics. Figure 8 shows the results from the individual PDE measurements with the direct (blue) and swapped (red) connection of the optical fibers. The systematic error due to optical contact, excluding a statistical contribution, is $\sim 1\%$ in absolute value.

At this point, it is possible to evaluate the photon detection efficiency of the device as the mean of all available measurements. The results are shown in fig. 9. The horizontal error bar is originated from the light source FWHM or filter bandwith; its impact on PDE evaluation gives the vertical error bar.

## 7. – Photon detection efficiency: CPTA sample

The noise and the signal spectra obtained with the CPTA sample, as shown in fig. 10 for $\lambda_w = 600 \pm 3\,\mathrm{nm}$, reflect the difference on the construction characteristics. With respect to the HAMAMATSU device fig. 10 (left) shows that with the chosen gate the

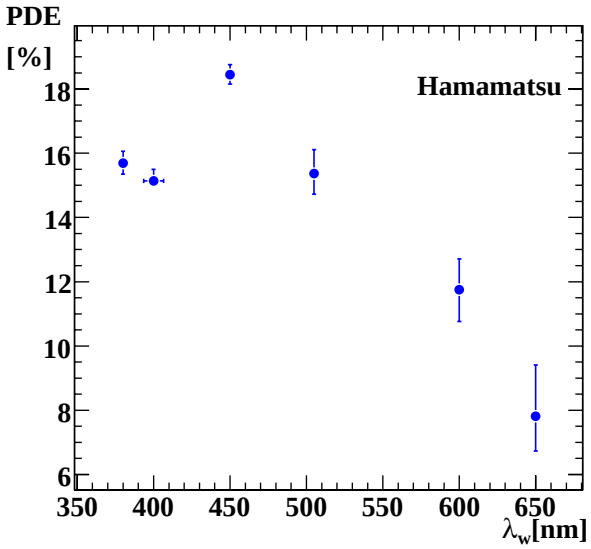


Fig. 9. – The photon detection efficiency, PDE, for the HAMAMATSU G-APD as a function of the light wavelength, $\lambda_w$.

thermogeneration is at a level of $\sim 30\%$, and fig. 10 (right) shows that the after-pulses have lower impact on the single photon spectra. The cross-talk effect is much lower.

The fit procedure adopted for the CPTA device is slightly different from that described in sect. **5**. The thermogeneration contribution was not included in the fit by excluding the region between the pedestal and one photoelectron peak, that is between 2 $\sigma$ from pedestal on the lower bound and 2 $\sigma$ from first peak on the upper bound.

In the use of eq. (4) the AP terms were not directly related to an after-pulse effect but accounted also for the thermogeneration and other effects. The result of the fit to the data of fig. 10 (right) is shown in fig. 11 (top) as a continuous line.

The $P_n^0$ values obtained were reported in fig. 11 (bottom), black dots, and fitted with Poisson's distribution. The mean number of photons detected is $N_\gamma^{\text{G-APD}} = 2.668 \pm 0.005$.

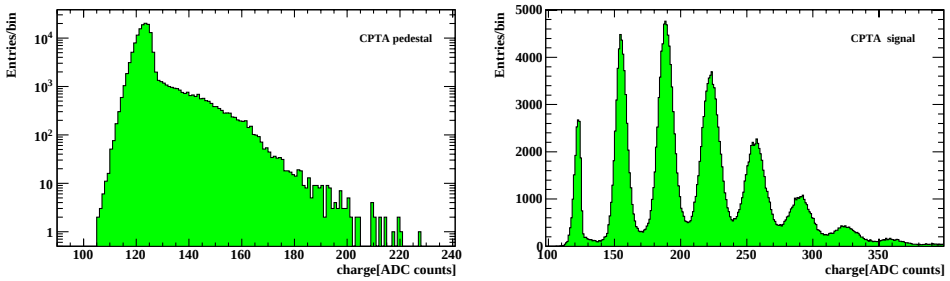


Fig. 10. – The noise (left) and signal (right) spectra obtained with the CPTA G-APD illuminated by short, low intensity LED flashes at $\lambda_w = 600 \pm 3$ nm. Each peak corresponds to a number of detected photons.

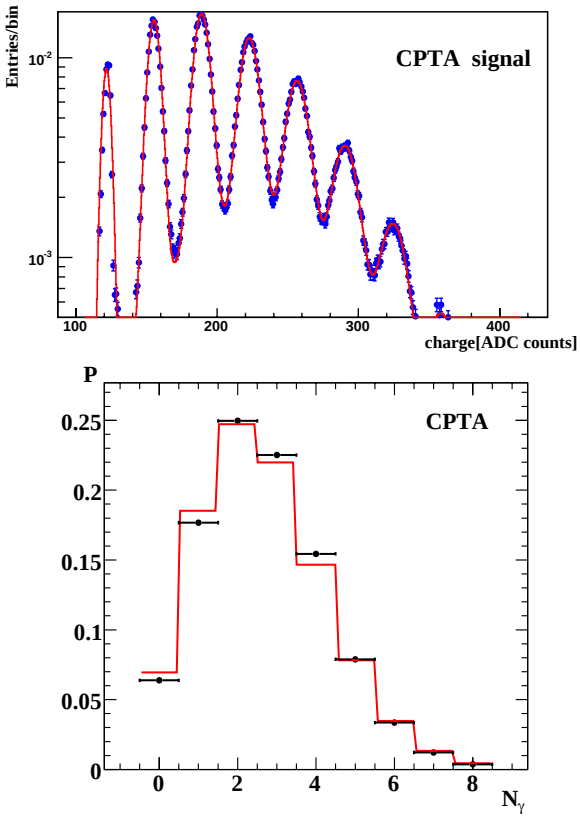


Fig. 11. – (Colour on-line) CPTA G-APD signal spectrum, at $\lambda_w = 600 \pm 3\,\mathrm{nm}$; the continuous line is the fit result (top). From the fit of the spectrum the probabilities, $P_n^0$, to get $n$ cells fired are obtained and plotted (bottom, black dots) with superimposed the fitted distribution (continuous red line). The fitted mean number of G-APD detected photons is $N_\gamma^{\text{G-APD}} = 2.668 \pm 0.005$. Binwidth = 1.

However, due to the low cross talk of this device, the fit method adopted has no sensitivity to this effect.

Taking into account that the detected number of photons from the reference detector, $N_\gamma^{\text{PMT}} = 0.666 \pm 0.007$, and the corresponding PMT reference detector efficiency, $\epsilon_{\text{eval}}^{\text{ref}} = 2.30^{+0.19}_{-0.19}\%$, the PDE value is $9.22 \pm 0.10\%$ (statistical error only).

The PDE results for other wavelengths are shown in fig. 12. The horizontal error bar is originated from the light source FWHM or filter bandwidth, the vertical one from its impact on the PDE evaluation. The measurements have been recorded at $V_{\text{bias}} = 32.5\,\text{V}$ for $\lambda_w = 450\,\text{nm}$, $565\,\text{nm}$, $600\,\text{nm}$ and $V_{\text{bias}} = 32.7\,\text{V}$ for $\lambda_w = 500\,\text{nm}$ and $600\,\text{nm}$. The measurement at $\lambda_w = 600\,\text{nm}$ has been recorded at both voltages.

**7˙1.** *Parameter dependence on overvoltage: gain.* – The PDE value varies with bias voltage, $V_{\text{bias}}$, or more precisely as a function of overvoltage, $V_{\text{bias}} - V_{\text{brd}}$, fig. 13. Then, the breakdown voltage of the device, $V_{\text{brd}}$, can be determined. This is done by measuring the G-APD gain, $g$, as a function of $V_{\text{bias}}$. Signal spectra (see for example fig. 11, top)

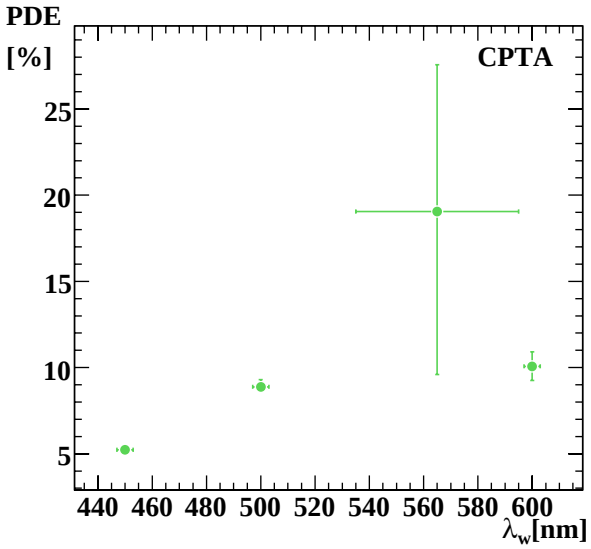


Fig. 12. – The photon detection efficiency, PDE, for CPTA G-APD as a function of the light wavelength, $\lambda_w$. The measurements at 450 nm, 565 nm, 600 nm have been recorded at $V_{\rm bias} = 32.5\,{\rm V}$, those at 500 nm, 600 nm at $V_{\rm bias} = 32.7\,{\rm V}$. The $\lambda_w = 600\,{\rm nm}$ measurements at the two bias voltages are indistinguishable. The error bars at $\lambda_w = 565\,{\rm nm}$ reflect the FWHM of light source, table I.

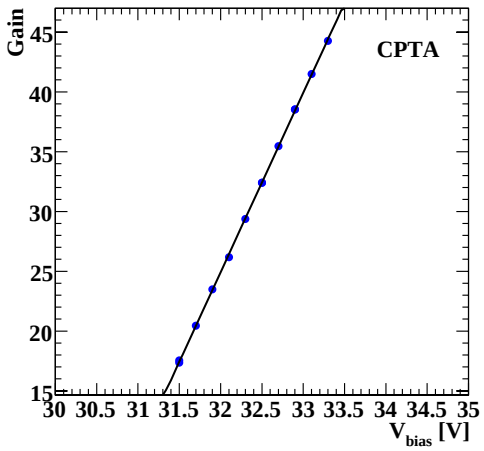


Fig. 13. – Gain (in ADC counts) in dependence on bias voltage, $V_{\rm bias}$, for CPTA G-APD. The breakdown voltage can be calculated extrapolating the curve to zero gain. The straight line fit parameters (Gain $= p_0 + p_1 V_{\rm bias}$) are $p_0 = -454.90 \pm 0.37$, $p_1 = 14.99 \pm 0.01\,{\rm V}^{-1}$.

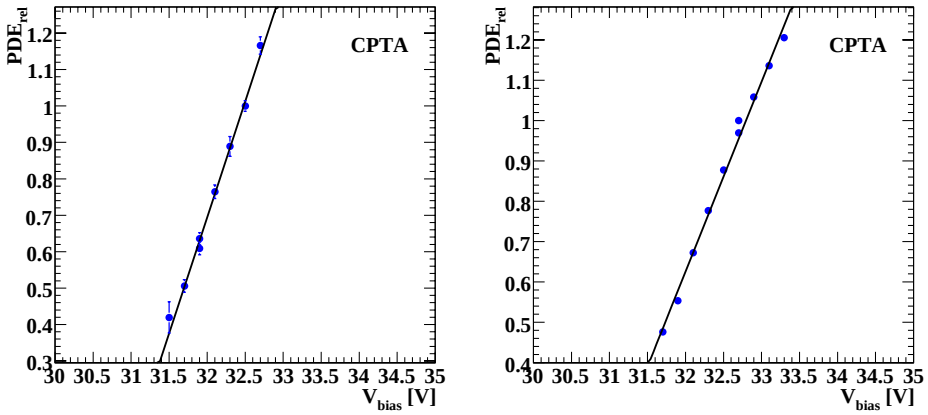


Fig. 14. – $\mathrm{PDE_{rel}}$, photon detection efficiency relative to the one at the reference voltage (fig. 12) as a function of $V_{\mathrm{bias}}$, for CPTA G-APD. The straight line fit ($\mathrm{PDE_{rel}} = p_0 + p_1 V_{\mathrm{bias}}$) angular coefficients are $p_1 = 0.64 \pm 0.02\,\mathrm{V}^{-1}$ ($\lambda_w = 450\,\mathrm{nm}$, left) and $0.470 \pm 0.001\,\mathrm{V}^{-1}$ ($\lambda_w = 500\,\mathrm{nm}$, right). The number of detected photons, $N_\gamma^{\mathrm{G\text{-}APD}}$ has, of course, the same dependence.

are recorded for a number of bias voltages and the gain is extracted from the distance between photon peaks in the corresponding spectrum, fig. 11, top. Figure 13 shows that the gain dependence on $V_{\mathrm{bias}}$ can be fitted by a straight line, which is found also for all other sets of measurements. By extrapolating this straight line to zero gain the value of breakdown voltage is estimated to be $V_{\mathrm{brd}} \sim 30.4\,\mathrm{V}$.

**7˙2.** *Parameter dependence on overvoltage: PDE.* – The photon detection efficiency, $\mathrm{PDE_{rel}}$, relative to the one at the reference voltage (fig. 12) is shown in fig. 14 as a function of $V_{\mathrm{bias}}$ for measurements recorded at two different wavelengths. From a straight line fit ($\mathrm{PDE_{rel}} = p_0 + p_1 V_{\mathrm{bias}}$) to other similar distributions the following values for the angular coefficients, $p_1$ ($\mathrm{V}^{-1}$), are derived: $p_1 = 0.64 \pm 0.02$ ($\lambda_w = 450\,\mathrm{nm}$), $p_1 = 0.470 \pm 0.001$ ($\lambda_w = 500\,\mathrm{nm}$), $p_1 = 0.51 \pm 0.01$ ($\lambda_w = 565\,\mathrm{nm}$), $p_1 = 0.52 \pm 0.01$ ($\lambda_w = 600\,\mathrm{nm}$).

From these slopes it is possible to calculate PDE as a function of $\lambda_w$ at various values of $V_{\mathrm{bias}}$, fig. 15. The validity of the method is tested with the measurements at 600 nm, taken at two different bias voltages. The value of PDE extrapolated at $V_{\mathrm{bias}} = 32.7\,\mathrm{V}$ is $(10.09 \pm 0.08)\%$ nicely consistent with the measured value $(10.07 \pm 0.09)\%$.

**7˙3.** *An improved fit procedure.* – The CPTA G-APD measurements described above have two peculiar aspects that deserve more attention: the thermogeneration effect is not negligible (fig. 10 (left) and fig. 16) and the after-pulse effect requests a dedicated treatment.

As a first step the thermogeneration spectrum shape is determined as a deviation of the noise spectrum, fig. 16, from a Gaussian. A combination of two exponential functions results into an appropriate description of this effect.

As a second step the fit of the signal pedestal, fig. 17 (top), is not performed with a simple Gaussian as above, but includes also the fit function determined in the first step and describing the thermogeneration. It is not anymore necessary to exclude from the fit the region between the pedestal and one photoelectron peak. This is nicely confirmed from fig. 17 (top).

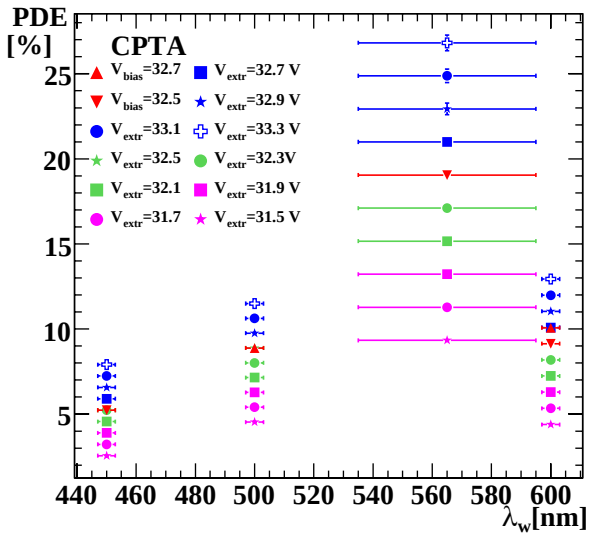


Fig. 15. – (Colour on-line) The photon detection efficiency, PDE, for the CPTA detector as a function of the wavelength, $\lambda_w$, as measured (red points, $V_{\rm bias} = 32.7$ and 32.5 V) and extrapolated (green, blue, magenta points).

Further improvement in the signal fit is achieved, if the after-pulse effect is modeled for a single fired pixel, as suggested in sect. **2**. The probability to have an after-pulse with delay time in $t$–$(t + {\rm d}t)$, with respect to the main pulse, can be written as

$$P^{\rm AP}(t) = \epsilon_{\rm Geiger} \times P_c \times \frac{e^{-t/\tau}}{\tau}\,,$$

where $\epsilon_{\rm Geiger}$ is the probability to trigger a Geiger discharge and $P_c$ is the probability that a carrier generated in an avalanche is subsequently trapped in a lattice defect and released later with the characteristic time constant, $\tau$, when the avalanche is alreadyquenched.

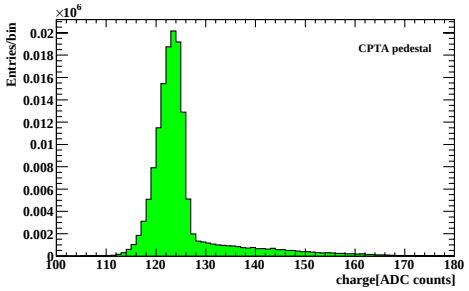


Fig. 16. – The CPTA G-APD noise spectrum at $\lambda_w = 450 \pm 3\,{\rm nm}$.

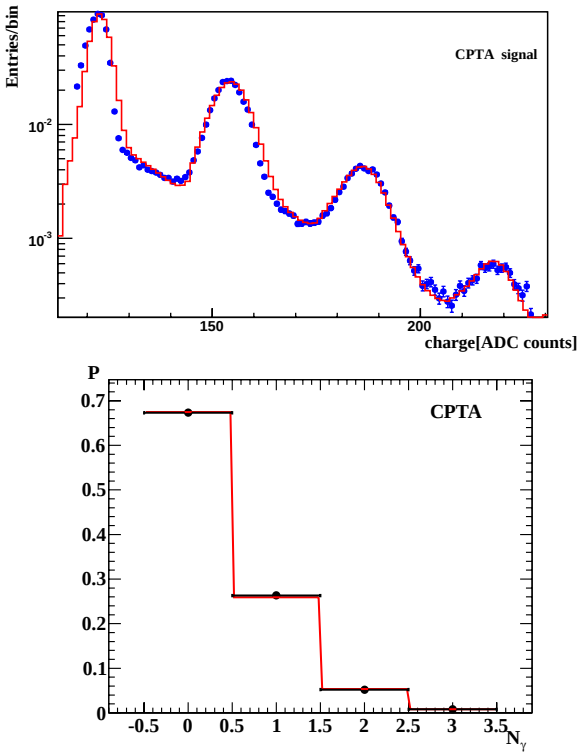


Fig. 17. – (Colour on-line) The CPTA G-APD signal spectrum (at $\lambda_w = 450 \pm 3\,\mathrm{nm}$) fitted with the improved fit procedure, subsect. **7**˙3, top. From the fit of the spectrum the probabilities, $P_n^0$, to get $n$ cells fired are obtained and plotted (bottom, black dots) with superimposed the fitted distribution (continuous red line). In this example, the AP probability is $P^{\mathrm{AP}} = (1.164 \pm 0.015)\%$, the fitted number of detected photons is $N_\gamma^{\text{G-APD}} = 0.014 \pm 0.003$, the cross-talk probability is $\varepsilon = 0.996 \pm 0.008\%$.

The amplitude $\mu(t)$ of this after-pulse can be approximated by an exponential law as

$$\mu(t) = g(1 - e^{-\alpha \cdot t}), \tag{7}$$

where $g$ is the gain and $1/\alpha$ can be identified as a recovery time. The effect, in eq. (7), as anticipated in sect. **2**, is proportional to the gain, in other words to the number of electrons. Moreover, the after-pulses coming soon after the main signal have smaller amplitude, since the pixel had no sufficient time to complete the recharge. Then it is possible to write

$$\frac{\mathrm{d}P^{\mathrm{AP}}}{\mathrm{d}\mu} = \frac{\mathrm{d}P^{\mathrm{AP}}}{\mathrm{d}t} \cdot \frac{\mathrm{d}t}{\mathrm{d}\mu} = A \times (g - \mu)^{\gamma},$$

where $\gamma = \frac{1}{\alpha \cdot \tau} - 1$, and $A$ is a normalization constant. The normalization costant $A$ is

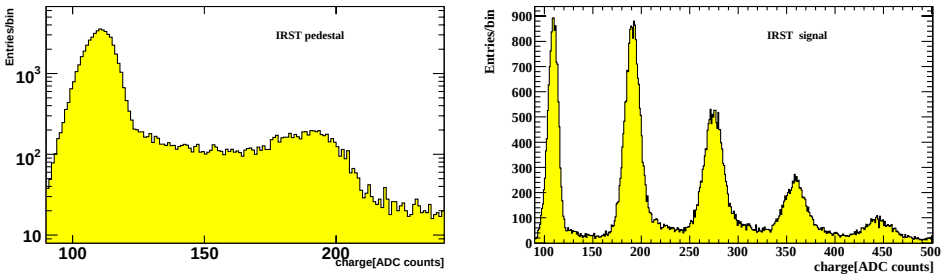


Fig. 18. – The noise (left) and signal (right) spectra obtained with the IRST G-APD illuminated by short, low intensity LED flashes at $\lambda_w = 600 \pm 3\,\mathrm{nm}$. Each peak corresponds to a number of photons.

obtained imposing

$$\int_0^g \frac{\mathrm{d}P^{\mathrm{AP}}}{\mathrm{d}\mu}\mathrm{d}\mu = 1.$$

The normalized distribution,

$$f_{\mathrm{AP}}(\mu) = \frac{\gamma+1}{g}\left(1-\frac{\mu}{g}\right)^{\gamma},$$

folded with a Gaussian distribution, $f_{\mathrm{AP}}(\mu) \otimes \mathrm{Gauss}(\mu,\sigma)$, can explicitly written as

$$\frac{\gamma+1}{g} \times \left(\frac{1}{\sqrt{2\pi}\sigma}\right) \int_0^g \left(1-\frac{\mu}{g}\right)^{\gamma} \times \exp\left[\frac{-(x-\mu)^2}{2\sigma^2}\right] \mathrm{d}x. \tag{8}$$

In this approach, in eq. (4) the $P_n^{\mathrm{noAP}}$ term takes into account the new pedestal fit with thermogeneration, and the $P_n^{\mathrm{AP1}}$, $P_n^{\mathrm{AP2}}$ terms are replaced by only one term $P_n^{\mathrm{AP}}$:

$$P_n^{\mathrm{AP}} = P_n^0 \times \left(f_{\mathrm{AP}}(\mu) \otimes \mathrm{Gauss}(\mu,\sigma)\right)\left(1-(1-P_{\mathrm{AP}})^n\right).$$

The results of this improved method are shown in fig. 17 (top) and the corresponding distribution of the number of photons in fig. 17 (bottom).

Using this fit procedure it is possible to derive a value of the cross-talk probability for the CPTA sample and the average obtained on measurements performed at many light intensities is $\leq 1.7\%$.

## 8. – IRST sample properties

Similar measurements were recorded with a IRST device, see for an example fig. 18. Again, the noise and signal spectra reflect the difference on construction and design. These spectra were recorded varying the voltage $V_{\mathrm{bias}}$, and for each value the gain was extracted, as in sect. **7**. The value of the breakdown voltage was determined in a series of measurements ($V_{\mathrm{brd}} \simeq 30.5$ V), fig. 19.

From fig. 18 and similar ones we have concluded that the specimen used was not suitable for PDE measurements.

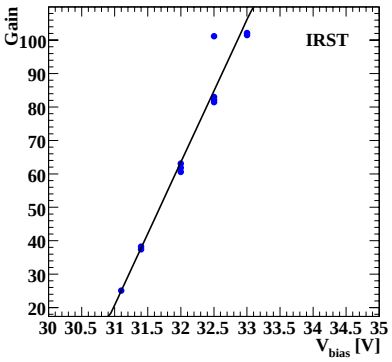


Fig. 19. – Gain dependence on bias voltage, $V_{\text{bias}}$ for IRST G-APD. The breakdown voltage can be calculated extrapolating the curve to zero gain. The straight line fit parameters (Gain = $p_0 + p_1 V_{\text{bias}}$) are $p_0 = -1301 \pm 0.48$, $p_1 = 42.65 \pm 0.02\,\text{V}^{-1}$.

## 9. – Conclusion

Measurements of G-APD response to low intensity light were recorded to determine the main characteristics of three different samples, HAMAMATSU (S10362-11-025U), CPTA, IRST. An accurate method to fit the response has been realized, to evaluate photon detection efficiency, cross-talk, gain, and after-pulse probability. A calibrated reference detector has been used for the photon detection efficiency measurements in a wavelength range between 380 and 650 nm.

The measurements were carried on in the same experimental condition (setup, thermal insulation ...) to compare the properties of various samples. This information is an important issue in the near future to identify the most suitable device for a particular application in high-energy physics calorimeters, astroparticle physics and medical environment.

The PDE measurements provided are consistent with those quoted from the manufacturers with a *caveat* due to the different method of measurement (the current method, very often used by manufacturers, includes after-pulse and cross-talk effects).

* * *

We would like to thank Profs. M. Danilov and E. Tarkovsky for the samples provided and clarifying discussions, Dr. I. Polak for having provided a fundamental part of electronics, and Prof. M. Fidecaro for comments to the manuscript.

REFERENCES

[1] Bondarenko G. *et al.*, *Nucl. Phys. Proc. Suppl. B*, **61** (1998) 347.
[2] Buzhan P. *et al.*, *Nucl. Instrum. Methods A*, **504** (2003) 48.
[3] Golovin V. and Saveliev V., *Nucl. Instrum. Methods A*, **518** (2004) 560.
[4] Dolgoshein B. *et al.*, *Nucl. Instrum. Methods A*, **563** (2006) 368.
[5] Yamamoto K. *et al.*, *IEEE Nucl. Sci. Symp. Conf. Rec.*, **2** (2006) 1094.
[6] Dinu N. *et al.*, *Nucl. Instrum. Methods A*, **572** (2007) 422.
[7] Bonanno G. *et al.*, *Nucl. Instrum. Methods A*, **610** (2009) 93.

[8] Danilov M., *Nucl. Instrum. Methods A*, **604** (2009) 183.
[9] Danilov M., *Nucl. Instrum. Methods A*, **581** (2007) 451.
[10] Heering A. *et al.*, *Nucl. Instrum. Methods A*, **576** (2007) 341.
[11] Orme D. *et al.*, to be published in *Nucl. Instrum. Methods A*.
[12] Teshima M., Dolgoshein B., Mirzoyan R., Nincovic J. and Popova E., *SiPM Development for Astroparticle Physics Applications*, arXiv:astro-ph/0709.1808 (2007).
[13] Otte N. *et al.*, *Nucl. Phys. Proc. Suppl.*, **150** (2006) 144.
[14] Mirzoyan R. *et al.*, *Nucl. Instrum. Methods A*, **572** (2007) 493.
[15] Otte N. *et al.*, *Nucl. Phys. Proc. Suppl.*, **150** (2006) 417.
[16] Piemonte C., *Nucl. Instrum. Methods A*, **568** (2006) 224.
[17] Hamamatsu Photonics K. K., Product catalogue No. KAPD0002E02 (2007).